



Type of article

Estimation of Vital Parameters of Glioblastoma Multiforme Growth Dynamics from a Model with Explicit Birth and Death Rates

Lifeng Han¹, Steffen Eikenberry¹, Chaghan He¹, Lauren Johnson¹, Mark C. Preul², Eric J. Kostelich¹, and Yang Kuang^{1, *}

¹ School of Mathematical and Statistical Sciences, Arizona State University, Tempe, AZ 85287, USA

² Department of Neurosurgery, Barrow Neurological Institute, St. Josephs Hospital and Medical Center, Phoenix, AZ 85013, USA

* **Correspondence:** kuang@asu.edu

Abstract: Glioblastoma multiforme (GBM) is an aggressive primary brain cancer with a grim prognosis. Its morphology is heterogeneous, but prototypically consists of an inner, largely necrotic core surrounded by an outer, contrast-enhancing rim, and often extensive tumor-associated edema beyond. This structure is usually demonstrated by magnetic resonance imaging (MRI). To help relate the three highly idealized components of GBMs (i.e. necrotic core, enhancing rim, and maximum edema extent) and to the underlying growth “laws,” a mathematical model of GBM growth with explicit motility, birth, and death processes is proposed. This model generates a traveling wave solution that mimics cancer progression. We develop several novel methods to approximate key characteristics of the wave profile, which can be compared with MRI data. Several simplified forms of growth and death terms and their parameter identifiability are studied. We use several test cases of MR image data of GBM patients to yield personalized parameterizations of the model, and the biological and clinical implications are discussed.

Keywords: Glioblastoma multiforme modeling; parameter estimation; traveling wave; necrosis; proliferation

1. Introduction

Glioblastoma multiforme (GBM) is a highly aggressive brain cancer, and the most malignant primary brain cancer, with median survival time from diagnosis on the order of 15 months, and long-term survival extremely rare [19]. Such rapid progression is promoted by highly proliferative and diffusely invasive cancer cells, with the diffuse nature of invasion rendering complete surgical cure rare. Magnetic resonance imaging (MRI) is conventionally used to identify the location and characteristics of the

tumor pre-operatively, guide surgery, and monitor and track progression or treatment response. Perioperatively, MRI is used to guide the resection of the tumor mass, and then for post-operative assessment of the volume of tumor resected, and to target other adjunct treatment such as radiation therapy.

GBMs morphologically typically appear (at least at initial diagnosis) as roughly spherical but highly heterogenous masses, that can often exhibit a (crudely speaking) three-layer structure. Within the tumor there is usually extensive cell necrosis, often accompanied by tumor cells, and a cystic component as well. An outer region, which typically appears as contrast-enhancing on T1-weighted gadolinium contrast-enhanced MRI, is cytologically typified by proliferating cells that then infiltrate into surrounding brain tissue. The surrounding brain tissue is generally seen to be edematous on T2-weighted or T2-FLAIR MRI and at operation, due to vasogenic edema. Within the edema area isolated or small aggregates of tumor cells can be found, and the region of edema has previously been interpreted as a surrogate for low-density infiltrative GBM cells [26].

Standard care for GBM patients was largely established with the seminal 2005 trial by Stupp et al. [24], and consists of following maximal surgical resection of the primary tumor, six weeks of radiation to the gross tumor volume, plus a 2–3 cm margin, with concomitant oral temozolamide (TMZ), and followed by six months to one year of maintenance TMZ chemotherapy [8]. Maximal surgical resection also appears to offer some survival benefit. Nevertheless, the absolute survival benefit even to the most effective therapy is generally measured only in months, and the highly infiltrative nature of GBMs makes recurrence, even with maximal resection and aggressive adjuvant therapy, nearly inevitable, although individual tumors may vary in the degree of invasiveness.

Given the grim situation, mathematical modeling has been proposed as a method to better understand the biophysical rules underlying GBM growth, with the ultimate goal to provide more effective therapy. Mathematical models have been widely applied to a variety of cancers, and cancer treatment in general (see [14]), with GBM is the focus of many such works (see [16] for a review). A popular class of cancer models takes the form of a system of reaction-diffusion equations. In many cases [9, 7, 23], such systems generate a traveling wave solution, with the traveling wave speed of great interest, as it is an indicator of how fast the cancer progresses.

However, models which confront the heterogeneity of GBM directly by utilizing spatiotemporal patient-specific data are rare. Swanson and colleagues [26, 18, 10] have employed variants of the well-known Fisher's equation to study cancer cell proliferation (P) and invasion (I) dynamics [6] (hence called PI model in [10]), with net growth and diffusion parameters estimated from two sequential patient MR images. The basic PI model is given mathematically as

$$\frac{\partial c}{\partial t} = \nabla \cdot [D \nabla c] + \rho c \left(1 - \frac{c}{K}\right), \quad (1.1)$$

where $c(x, t)$ is cancer cell density at location x and time t , with D the diffusion coefficient and ρ the intrinsic tumor cell growth rate. The model can yield a living tumor core and an advancing front, but cannot capture any heterogeneity between live and necrotic tumor cells. While several modeling effort take into account a variety of proliferating, migrating, or necrotic cell components [4, 25], they are usually too complicated to be parameterized to a single (or very limited number of) patient MRI series. Thus, the motivation for this work is to extend the baseline PI model to include necrotic cells in a very simplified way, such that three idealized components of a GBM seen on imaging (described below) can be related to model parameters, and these parameters may be uniquely identified from just one or two MRIs.

As above, MRI only indirectly shows cancers cells and GBMs are highly heterogeneous, but T1-weighted sequences often show a (partially) necrotic core region surrounded by a bright enhancing rim that correlates with high blood vessel density, and presumably, rapid cell proliferation. This core and rim is usually surrounded by a large expanse of edema that is best visualized on T2-weighted MRI, and has been found to harbor and correspond with a component of diffusely invasive, highly motile GBM cells, as presumed in much of the work by Swanson et al. [26]. Thus, we can extract, in the best case and approximating the tumor as a sphere, three *idealized* digital marks from imaging: Necrotic radius, enhancing radius, and what we shall refer to as the T2 or maximum radius. We hypothesize that a relatively simple mathematical model framework may capture all these three digital marks, and thus yield insights into the relative contributions of cellular proliferation, motility, and necrosis to the observed image features.

The paper is organized as following. We first describe our model and its assumptions. We then demonstrate that the model has a traveling wave solution and present the approximate wave profile. We further devise a simple procedure to estimate patient-specific parameters by fitting the approximate wave profile to a tumor profile derived from patient MRIs. Identifiability of parameters is also discussed, and we apply this parameter estimation procedure to obtain the cancer vital dynamics parameters (consisting of the rate of cancer cell proliferation, death and diffusion) for several patients.

2. Model and method

2.1. Model description

To model the growth of GBM, we propose a system of reaction-diffusion equations

$$\frac{\partial p}{\partial t} = \nabla \cdot \left[\frac{Dp}{p+q} \nabla(p+q) \right] + \tilde{g}(w)p - \tilde{\delta}(w)p, \quad (2.1a)$$

$$\frac{\partial q}{\partial t} = \nabla \cdot \left[\frac{Dq}{p+q} \nabla(p+q) \right] + \tilde{\delta}(w)p, \quad (2.1b)$$

where

$$w = 1 - p - q, \quad (2.2)$$

and proliferating and quiescent (or necrotic) cell densities at time t and location x are represented by $p(x, t)$ and $q(x, t)$, respectively; quiescent cells are functionally equivalent to necrotic cells in this framework. We assume the flux of total population due to migration is $-D\nabla(p+q)$ where D is a constant diffusion coefficient. It is further assumed that the proportion of the total flux contributed by each species equals their proportion of the total population, based on the model in [21].

Per capita birth rate is $\tilde{g}(w)$ and the proliferating cells become quiescent with per capita rate $\tilde{\delta}(w)$, where w , defined as $w = 1 - p - q$, represents the availability of space or some generic nutrient (we call it growth factor henceforth). By doing so, we have scaled the maximum cell density to be 1. In our model, necrosis is not explicitly included, but again, can be regarded as being lumped into q . Moreover, as quiescent cells can not become proliferating again, $\tilde{\delta}(w)$ can be viewed as a (functional) death rate. Our motivation in keeping the model framework relatively simple is to estimate model parameters directly from sparse clinical MRI imaging.

To make the model biologically reasonable, we impose the following constraints on $g(w)$ and $\delta(w)$:

$$\tilde{g}'(w) \geq 0, \tilde{\delta}'(w) \leq 0, \tilde{g}(1) \geq \tilde{\delta}(1) = 0, \tilde{\delta}(0) > \tilde{g}(0) = 0. \quad (2.3)$$

That is, birth (death) should increase (decrease) with availability of the growth factor, there is more birth than death at maximum growth factor, and there is only death with no growth in absence of growth factor. It is also assumed that the death rate is negligible at maximum growth factor. With these assumptions, we observe numerically that with suitable initial conditions, the solution of (2.1) stays positive and is bounded ($p + q \leq 1$) for all t .

We can only estimate up to three parameters based on the three pieces of information we can derive from MRI images (discussed below). Therefore we want a few more restrictions on $\tilde{g}(w)$ and $\tilde{\delta}(w)$ for the ease of parameter estimation and ensure their identifiability. Since we can only introduce two more parameters in addition to diffusion coefficient D , we introduce ρ and k into $\tilde{g}(w)$ and $\tilde{\delta}(w)$ respectively and indicate their dependence on the parameters as $\tilde{g}(w; \rho)$ and $\tilde{\delta}(w; k)$. It is desirable to make the proliferating rate at maximum growth factor be ρ and death rate at zero growth factor be k , i.e., $\tilde{g}(1, \rho) = \rho$, $\tilde{\delta}(0; k) = k$. For reasons that will become clear later, we pick the functional form which can be written as $\tilde{g}(w; \rho) = \rho g(w)$ and $\tilde{\delta}(w; k) = k \delta(w)$. Some examples of $g(w)$ and $\delta(w)$ include the cumulative distribution function of beta distribution family (see left pane of Figure 4). Although we have stated several additional assumptions, it should be noted that they impose little impact on the generality and flexibility of our model. The benefit of including them will become clear in the section of parameter estimation.

2.2. Approximate wave profile

In most biological applications of reaction-diffusion models, solutions quickly take the form of traveling waves. MRI images of GBM cancer growth suggests we can approximate the cancer population growth curve by a traveling wave solution of its growth model. In order to uniquely identify and accurately approximate GBM growth model parameters, it is highly desirable to obtain some analytic approximation of the travel wave so a computational match of the image wave profile and the approximate model wave profile can be made. To this end and for simplicity, we consider one spatial dimension. It is justified by the fact that the tumor is mostly spherical and at the time of diagnosis its radius is large enough so that radial effect is negligible. Together with the aforementioned assumptions, the equations may take the following forms:

$$\frac{\partial p}{\partial t} = \frac{\partial}{\partial x} \left[\frac{Dp}{p+q} \frac{\partial}{\partial x} (p+q) \right] + \rho g(w)p - k\delta(w)p, \quad (2.4a)$$

$$\frac{\partial q}{\partial t} = \frac{\partial}{\partial x} \left[\frac{Dq}{p+q} \frac{\partial}{\partial x} (p+q) \right] + k\delta(w)p. \quad (2.4b)$$

We nondimensionlize the system using the characteristic length $\sqrt{D/k}$ and the characteristic time $1/k$ so that $x = \sqrt{D/k}\hat{x}$ and $t = \hat{t}/k$, which leads to

$$\frac{\partial p}{\partial \hat{t}} = \frac{\partial}{\partial \hat{x}} \left[\frac{p}{p+q} \frac{\partial}{\partial \hat{x}} (p+q) \right] + \hat{\rho} g(w)p - \delta(w)p, \quad (2.5a)$$

$$\frac{\partial q}{\partial \hat{t}} = \frac{\partial}{\partial \hat{x}} \left[\frac{q}{p+q} \frac{\partial}{\partial \hat{x}} (p+q) \right] + \delta(w)p, \quad (2.5b)$$

where $\hat{\rho} = \rho/k$. We are seeking a traveling wave solution, i.e., $p(\xi) = p(\hat{x} - c\hat{t})$, $q(\xi) = q(\hat{x} - c\hat{t})$ where c is wave speed. Substituting these into (2.5) gives

$$\left(\frac{p}{p+q}(p+q)'\right)' + cp' + \hat{\rho}g(w)p - \delta(w)p = 0, \quad (2.6a)$$

$$\left(\frac{q}{p+q}(p+q)'\right)' + cq' + \delta(w)p = 0, \quad (2.6b)$$

where the prime indicates the derivative with respect to ξ . Linearizing at the wave head, i.e., substitute an ansatz $p = Ae^{-r\xi}$ and $q = Be^{-r\xi}$ into (2.6) gives $(r^2 - cr + \rho)A = 0$. For a biologically realistic wave front, we expect $A > 0$, $B > 0$ and $r > 0$. This requires that $c^2 > 4\rho$, which implies that the minimum speed of the wave $c_{\min} = 2\sqrt{\hat{\rho}}$. It is numerically verified that the minimum speed is exactly the asymptotic speed, i.e., $c = c_{\min}$.

To obtain a approximate wave profile, we adopt a popular method first used by Canosa in [2]. We rescale the wave coordinate $z = -\xi/c$, which leads to

$$\frac{1}{c^2}\left(\frac{p}{p+q}(p+q)'\right)' - p' + \hat{\rho}g(w)p - \delta(w)p = 0, \quad (2.7a)$$

$$\frac{1}{c^2}\left(\frac{q}{p+q}(p+q)'\right)' - q' + \delta(w)p = 0, \quad (2.7b)$$

where the prime indicates the derivative with respect to z . Assuming that $1/c^2$ is small, we neglect the first terms of (2.7a),(2.7b). Writing the system in terms of p and w , we obtain the following reduced system

$$\frac{dp}{dz} = p(\hat{\rho}g(w) - \delta(w)), \quad (2.8a)$$

$$\frac{dw}{dz} = -\hat{\rho}pg(w), \quad (2.8b)$$

which is amenable to phase plane analysis. The approximate wave solution corresponds to a trajectory that leaves $(0, 1)$ and ends at $(0, w^*)$ with $w^* \in [0, 1)$ (see Figure 1). Its existence based on assumptions (2.3) is shown in the appendix. Dividing (2.8a) by (2.8b) yields

$$\frac{dp}{dw} = \frac{\delta(w)}{\hat{\rho}g(w)} - 1. \quad (2.9)$$

Upon integration we get p as a function of w , i.e., $p = p(w)$, which we will make use of in the next section.

2.3. Parameter estimation

From clinical MRI data, we may derived three idealized radii, R_0 , R_1 and R_2 , representing the radius of the inner necrotic core, the radius to the edge of the contrast-enhancing rim, and the radius to the outer edge of tumor-associated edema. Such data was extracted from a series of anonymized patient

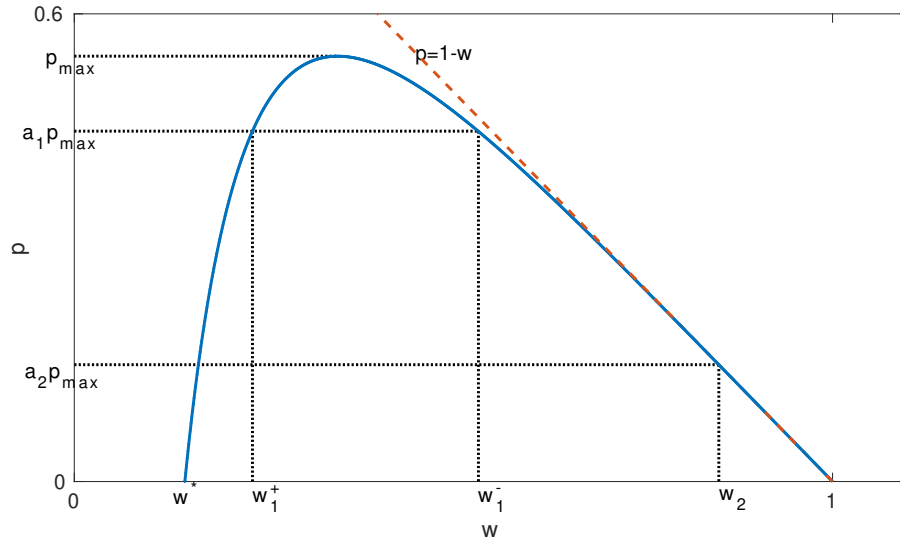


Figure 1. A typical trajectory that connects $(0,1)$ and $(0,w^*)$ in the phase plane. Given $\delta(w)$ and $g(w)$, this trajectory can be found by integrating (2.9). This trajectory represents an approximate traveling wave solution and its existence under general assumptions is shown in the appendix.

MRI data consisting of T1-contrast enhanced and T2-weighted MRIs at initial diagnosis. Using SPM 12, MRIs were initially registered to a standard brain space, and then, using Slicer 3D, the total necrotic core volumes, enhancing rim volumes, and tumor-associated edema volumes were determined from semi-manual tumor segmentation. Finally, these volumes were converted to radii assuming a spherical tumor geometry. The width of proliferating rim, denoted as L_1 , and the width of the edematous rim, denoted as L_2 , can be calculated as $L_1 = R_1 - R_0$ and $L_2 = R_2 - R_1$. This is demonstrated visually in Figures 2 and 3.

We follow [26] in assuming that T1-weighted contrast-enhancing images correlate only with high densities of proliferating tumor cells, while edema on T2-weighted imaging may correspond to low densities of proliferating tumor cells. We denote the respective detection thresholds for T1 and T2 imaging as $100 \times a_1\%$ and $100 \times a_2\%$ of $p_{\max} = \max_z \{p(z)\}$ (the actual maximum density of proliferating cells given by the traveling wave solution) with $a_1 > a_2$.

Often only a single MRI series is available before surgery, although in some cases a diagnostic MRI followed by a pre-surgery MRI some days or weeks later may be available [26]. In such a case, the image-derived wave velocity V is the change in tumor radius divided by the length of this time interval.

From our approximate wave profile, we can compute the corresponding quantities to match with images (Figure 3). The rim width (in dimensional form) is computed as below

$$\ell_1 = \frac{2\sqrt{D\rho}}{k} \int_{w_1^-}^{w_1^+} \frac{dz}{dw} dw, \quad (2.10a)$$

$$\ell_2 = \frac{2\sqrt{D\rho}}{k} \int_{w_2}^{w_1^-} \frac{dz}{dw} dw, \quad (2.10b)$$

where w_1^\pm and w_2 satisfy $p(w_1^\pm) = a_1 p_{\max}$, $p(w_2) = a_2 p_{\max}$ with $p(w)$ resulted from integration of (2.9) (see appendix for details). Additionally, model-derived wave speed $c = 2\sqrt{\rho D}$ can be matched with image-derived speed V . Thus we have three nonlinear equations

$$\{\ell_1 = L_1, \ell_2 = L_2, c = V\}, \quad (2.11)$$

from which we hope to find parameters D, ρ and k . Due to the assumptions we made before, we can simply take the ratio of (2.10a) and (2.10b), which gives

$$f(\hat{\rho}) \equiv \frac{\int_{w_1^-}^{w_1^+} \frac{dz}{dw} dw}{\int_{w_2}^{w_1^-} \frac{dz}{dw} dw} = \frac{L_1}{L_2}, \quad (2.12)$$

where we note that the integrals are functions of $\hat{\rho}$. Observe that (2.12) can be solved for $\hat{\rho}$ analytically in special cases or numerically in general. We note that the monotonicity of $f(\cdot)$ is important for identifiability of parameters. Once we find $\hat{\rho}$, i.e., the ratio ρ/k , all parameters can be found by back substitution.

The above method requires two MR scans taken at two consecutive times before surgery in order to obtain image-derived wave speed. If the second image is not available, another approximation can be made to deal with such a situation. Generally, tumor age can be estimated by the tumor radius divided by the wave speed. However, age estimation differs in terms of which radius (say R_1 or R_2) to use. This discrepancy can be explained by the common observation that tumor grows exponentially at the initial stage and then linearly later on [14]. This initial exponential growth stage needs to be taken into account as a correction to the aforementioned tumor age estimation. Assuming that from $t = 0$ to $t = t^*$, quiescence is negligible and the proliferating cancer cells grows exponentially from a point source of density p_0 , and that after $t = t^*$ the tumor grows as a traveling wave speed $2\sqrt{\rho D}$, we have

$$\frac{R_1 - R_1^*}{2\sqrt{\rho D}} = \frac{R_2 - R_2^*}{2\sqrt{\rho D}}, \quad (2.13)$$

by equating the two age estimations, where

$$R_i^* = t^* \sqrt{4D\rho - \frac{4D}{t^*} \ln\left(\frac{a_i}{p_0} (4\pi D t^*)^{3/2}\right)} \quad (2.14)$$

with $i = 1, 2$ are respectively T1 and T2 radius at $t = t^*$ (see details of R_1^* and R_2^* in the appendix).

Replacing the last equation in (2.11) with (2.13), we have again three equations. To solve these equations for the unknown parameters, we first take (2.10a) over (2.10b) same as previously and obtain (2.12). It can then be solved for the ratio $\hat{\rho} = \rho/k$. Substituting this back to either $\ell_1 = L_1$ or $\ell_2 = L_2$ gives the ratio ρ/D . Lastly, expressing D and k in terms of ρ , (2.13) can be solved for ρ , and D and k follow.

3. Results

We first investigate the monotonicity of $f(\cdot)$ for some specific choice of $g(w)$ and $\delta(w)$ because it is crucial for parameter identifiability. Given our restrictions on $g(w)$ and $\delta(w)$, the cumulative density

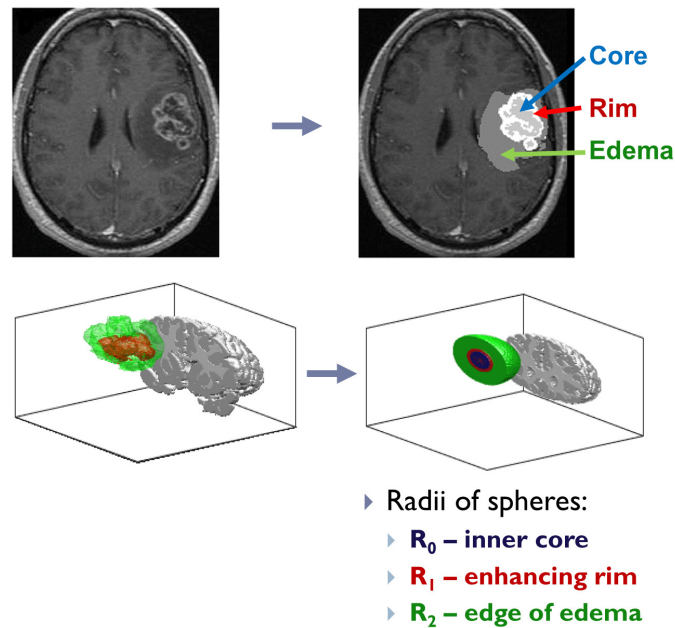


Figure 2. The top half of the figure shows an example patient MRI registered to the standard brain domain, with the three tumor segments, necrotic core, enhancing rim, and tumor-associated edema highlighted on a single 2-D slice. The full 3-D segmentation, and the equivalent tumor sphere with associated radii, R_0 , R_1 , and R_2 , is shown on the figure lower half.

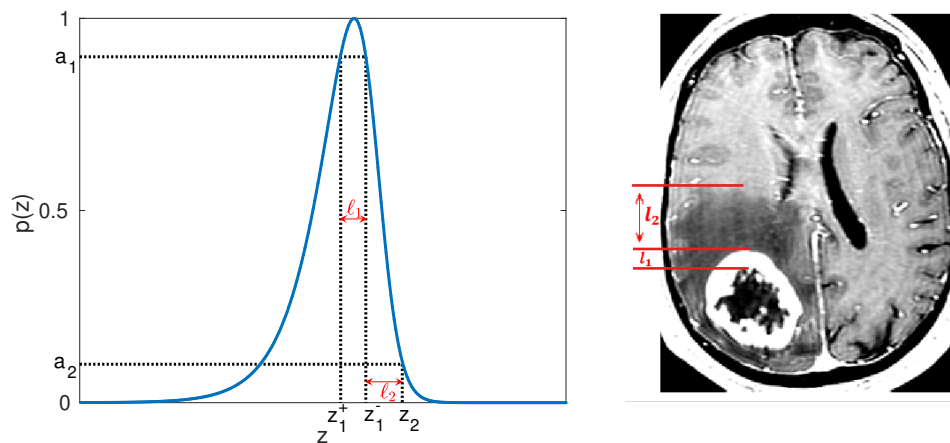


Figure 3. Left: normalized wave profile generated by the model in z -coordinate. Right: tumor profile seen in MR image. Parameter estimation is done by matching model-derived quantities, e.g., ℓ_1 and ℓ_2 , to the corresponding image-derived ones.

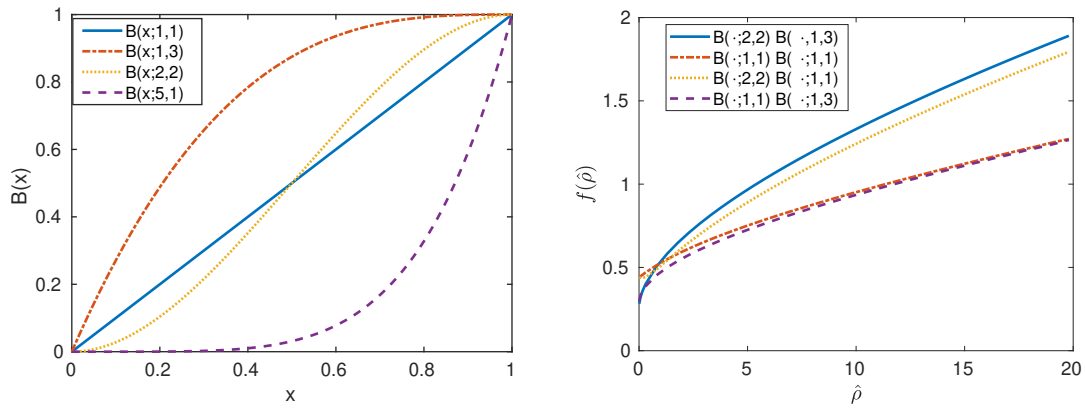


Figure 4. Left: CDF of some beta distribution. These functions satisfy (2.3) and serve as reasonable candidates to phenomenologically represent biological response to limitation of growth factors. Right: monotonicity of $f(\cdot)$ given different choices of $g(w)$ and $\delta(w)$ as indicated in the legend. All choices lead to monotonic function $f(\cdot)$ and hence identifiable parameters.

function (CDF) of the Beta distribution family suits our purposes. Therefore, we let $g(w) = B(w; \alpha_g, \beta_g)$ and $\delta(w) = 1 - B(w; \alpha_\delta, \beta_\delta)$, where $B(w; \alpha, \beta)$ is the CDF of Beta distribution with shape parameters α and β . By tweaking α and β , we can get linear, sigmoid and concave up/down curves (see left pane of Figure 4). It turns out that our framework is very robust to those choices, i.e., monotonicity of $f(\cdot)$ is well preserved (right pane of Figure 4). As can be seen, the sigmoid shaped $g(w)$ and $\delta(w)$ give larger range of $f(\cdot)$ and thus more flexibility in parameter estimation. Moreover, sigmoid curves are believed to be biologically relevant (most enzymatic reaction rates have the same shape with respect to reactant concentration). Therefore, we focus on this choice and move on to find patient specific parameters using their MRIs.

We parameterize our model with patient data in which there is only one MRI scan before surgery. In Table 1 we summarize the image-derived tumor radii and the corresponding parameters estimated by the method introduced in the previous section. Hyperparameters $a_1 = 0.9$, $a_2 = 0.1$ are adapted from numbers found in the literature [26], while $p_0 = 0.02$ and $t^* = 60$ days are hypothetical values. We observe substantial variation of the parameters among individual patients.

We compare our approximate quantities to those obtained from the numerical solution of the model. As shown in Figure 5, the approximated results match with numerical results well except for some discrepancy for L_2 when $\hat{\rho}$ is small. It is not a surprise since the approximation is based on assumption of large $c = 2\sqrt{\hat{\rho}}$. Moreover, numerical approximation of L_2 is prone to errors due to the fixed grid size and large rate of change around the threshold of L_2 . Overall, we are convinced that our approximation is accurate for the parameter range arisen from the image data.

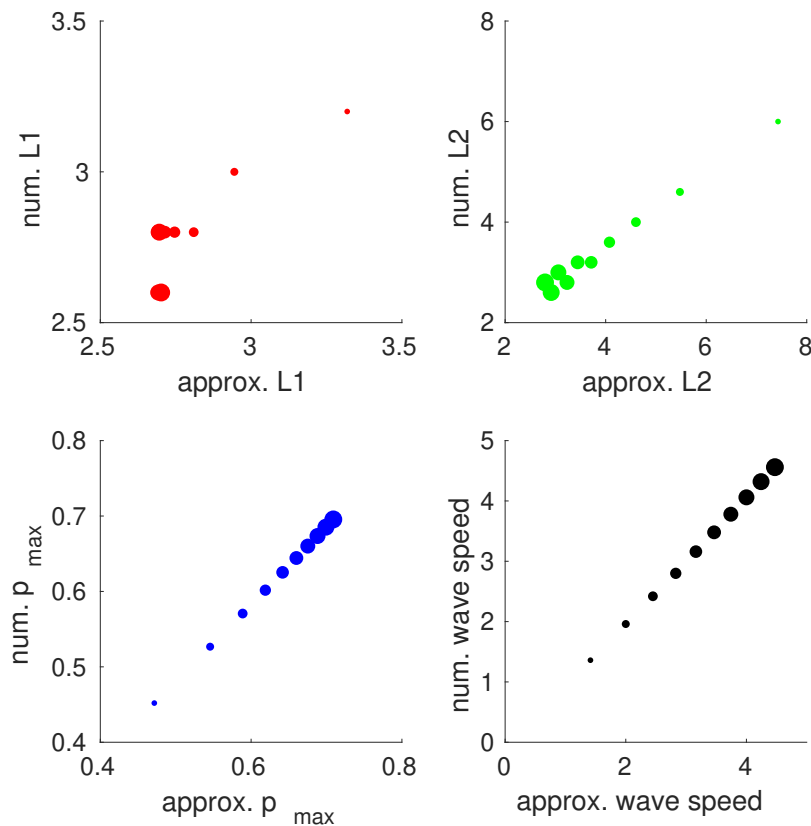


Figure 5. Scatter plots of approximate wave profile characteristics (on horizontal axis) verses the ones obtained by numerical simulation (on vertical axis) for a range of $\hat{\rho}$ from 0.5 to 5 by incremental 0.5. The size the the dot corresponds to the value of $\hat{\rho}$. The dots scatter closely to the diagonal line with slope 1, indicating agreement between the numerical solution and our approximation.

Table 1. Radii of equivalent tumor sphere derived from T1 and T2 images and the corresponding vital parameters estimated by our protocol. We have preset $a_1 = 0.9, a_2 = 0.1, p_0 = 0.02$ mm and $t^* = 60$ days.

Patient no.	R_0 , mm	R_1 , mm	R_2 , mm	D , mm ² day ⁻¹	ρ , day ⁻¹	k , day ⁻¹
1	14.87	20.73	27.77	0.2852	0.2102	0.0602
2	20.48	26.34	38.24	1.2791	0.2624	0.3537
3	6.61	10.91	15.24	0.0825	0.1736	0.0327
4	22.87	26.96	37.03	0.9825	0.2590	0.7819
5	8.17	14.20	25.10	0.9769	0.2520	0.2260
6	8.29	15.83	20.35	0.0687	0.1652	0.0106

4. Discussion

In this work we have extended the proliferation-invasion model previously used by Swanson et al. [26] to describe GBM growth by explicitly separating the cancer cell birth and death (or quiescence) processes, with these described via generic functions that depend upon an implicit nutrient or growth factor. We specify the birth and death processes, $g(w)$ and $\delta(w)$, respectively, by the CDF for a Beta distribution, each uniquely specified by a single parameter, ρ and k . Thus, along with the linear diffusion coefficient, D , our model describes cancer growth via three parameters, D , ρ , and k , and yields a tumor morphology (in one dimension) consisting of a necrotic core, a high-density rim, and an outer low density rim, which we may correlate to three radii, R_0 , R_1 , and R_2 , derived from actual patient MR imaging.

We have demonstrated a traveling wave solution to our reaction-diffusion system. Such a solution is not uncommon in a reaction-diffusion systems, and studies on this topic date back to the seminal work by Fisher on spread of advantageous genes [6]. Rigorous proof of the existence of traveling wave solution in a reaction-diffusion system often leads to phase space analysis such as the one on diffusive Lotka-Volterra equations [3]. Not only the high dimension but also the singularity represented in the cross diffusion makes any rigorous proof a daunting task. Nevertheless, the reduced system is amenable to phase plane analysis and the orbit representing the traveling wave solution can be identified (see appendix).

Via travelling wave analysis, we have developed a method to estimate D , ρ , and k from either the three tumor radii and a single estimate of tumor growth velocity, if two sequential MRIs are available, or to estimate all three directly from a single MRI under certain assumptions for growth. We have estimated these parameters for six patient test cases, as shown in Table 1. Because of the scarcity of individual patient's image data, parameter identifiability in this case is simply justified by the monotonicity of function $f(\cdot)$ as seen in left pane of Figure 4, which is in contrast from common statistical practices [5] when a fair amount of data are available.

Disaggregating the lumped proliferation term into birth and death processes not only aids in relating (simplified) tumor appearance on MRI, separating considering the rates of birth versus death, instead of a lumped net proliferation term, could also provide valuable information for personalized treatment design, since most chemotherapy and radiotherapy target proliferating cells. Moreover, the structural information is also potentially useful, e.g., it may help deciding drug dose so that the drug can perfuse through the width of the proliferating rim. Research along this general line has been conducted using the PI model [11].

We also use a slightly more complex description of motility than simple diffusion, with our diffusion term in (2.4) falling into a general category called cross diffusion [15]. This represents the phenomenon in which the gradient in the concentration of one species can cause a flux of another species. This type of cross diffusion considered here was studied in a more general and theoretical context [20], and in a modeling study of avascular tumour growth [21], the authors justified the adoption of this proportion-based cross diffusion in a tumor growth model by recognizing that tumor cell migration is “contact inhibited”, i.e., the presence of one type of cell prevents the movements of the other. Other types of density-dependent diffusion have also been considered in modeling GBM migration [22].

Despite the existence of many possible diffusion terms, we note that in our analysis the exact form of diffusion does not matter since the second derivatives are dropped in (2.7). The diffusion coefficient

does play an important role in the linearized wave head where it affects the wave speed, and in characteristic length where its square root scales the space. However, the scale invariant part of the wave profile is mostly determined by the exact forms of the birth and death functions.

The major contribution of this paper consists in presenting two novel methods of making use of scarce MRI data routinely available in clinical settings to estimate a three-parameter model for tumor growth. From a single pre-surgery MRI, patient-specific parameters can be estimated, while an improved estimated can be made if two MRIs are available. It is also straightforward to extend the current method to make use of MR images taken at three or even more time points, and conceivably even after resection of the tumor from MR imaging that shows tumor recurrence or expansion.

As cancers evolve, the underlying parameters describing their growth are likely to evolve as well. Data assimilation refers to basic method of updating parameters as more data is acquired, and there has been research on applying full-fledged data assimilation to cancer modeling [12, 17]. The method described in this paper could be incorporated into a data assimilation context in the future.

Acknowledgments

The authors would like to thank Leslie Baxter and Leland Ho at Barrow Neurological Institute for providing MR images. The work is supported by a grant from Arizona Biomedical Research Commission, and by funds from the Newsome Chair in Neurosurgery Research held by Dr. Preul.

References

1. N. F. Britton, *Essential mathematical biology*, Springer, 2003.
2. J. Canosa, On a Nonlinear Diffusion Equation Describing Population Growth, *IBM Journal of Research and Development*, **17** (1973), 307–313, URL <http://ieeexplore.ieee.org/document/5391351/>.
3. S. Dunbar, Travelling wave solutions of diffusive Lotka-Volterra equations, *Journal of Mathematical Biology*, **17** (1983), 11–32, URL <http://link.springer.com/10.1007/BF00276112>.
4. S. E. Eikenberry, T. Sankar, M. C. Preul, E. J. Kostelich, C. J. Thalhauser and Y. Kuang, Virtual glioblastoma: Growth, migration and treatment in a three-dimensional mathematical model, *Cell Proliferation*, **42** (2009), 511–528.
5. M. C. Eisenberg and H. V. Jain, A confidence building exercise in data and identifiability: Modeling cancer chemotherapy as a case study, *Journal of Theoretical Biology*, **431** (2017), 63–78, URL <https://www.sciencedirect.com/science/article/pii/S0022519317303454?via%3Dihub>.
6. R. A. Fisher, The wave of advance of advantageous genes, *Annals of Eugenics*, **7** (1937), 355–369, URL <http://doi.wiley.com/10.1111/j.1469-1809.1937.tb02153.x>.
7. P. Gerlee and S. Nelander, Travelling wave analysis of a mathematical model of glioblastoma growth, *Mathematical Biosciences*, **276** (2016), 75–81, URL <https://www.sciencedirect.com/science/article/abs/pii/S0025556416000602?via%3Dihub>.

8. M. R. Gilbert, M. Wang, K. D. Aldape, R. Stupp, M. E. Hegi, K. A. Jaeckle, T. S. Armstrong, J. S. Wefel, M. Won, D. T. Blumenthal, A. Mahajan, C. J. Schultz, S. Erridge, B. Baumert, K. I. Hopkins, T. Tzuk-Shina, P. D. Brown, A. Chakravarti, W. J. Curran and M. P. Mehta, Dose-dense temozolomide for newly diagnosed glioblastoma: a randomized phase III clinical trial., *Journal of clinical oncology : official journal of the American Society of Clinical Oncology*, **31** (2013), 4085–91, URL <http://ascopubs.org/doi/10.1200/JCO.2013.49.6968><http://www.ncbi.nlm.nih.gov/pubmed/24101040><http://www.pubmedcentral.nih.gov/articlerender.fcgi?artid=PMC3816958>.
9. K. Harley, P. van Heijster, R. Marangell, G. J. Pettet and M. Wechselberger, Existence of Traveling Wave Solutions for a Model of Tumor Invasion, *SIAM Journal on Applied Dynamical Systems*, **13** (2014), 366–396, URL <http://epubs.siam.org/doi/10.1137/130923129>.
10. P. R. Jackson, J. Juliano, A. Hawkins-Daarud, R. C. Rockne and K. R. Swanson, Patient-Specific Mathematical Neuro-Oncology: Using a Simple Proliferation and Invasion Tumor Model to Inform Clinical Practice, *Bulletin of Mathematical Biology*, **77** (2015), 846–856, URL <http://link.springer.com/10.1007/s11538-015-0067-7>.
11. M. Kim, J. Kotas, J. Rockhill, M. Phillips, M. Kim, J. Kotas, J. Rockhill and M. Phillips, A Feasibility Study of Personalized Prescription Schemes for Glioblastoma Patients Using a Proliferation and Invasion Glioma Model, *Cancers*, **9** (2017), 51, URL <http://www.mdpi.com/2072-6694/9/5/51>.
12. E. J. Kostelich, Y. Kuang, J. M. McDaniel, N. Z. Moore, N. L. Martirosyan and M. C. Preul, Accurate state estimation from uncertain data and models: an application of data assimilation to mathematical models of human brain tumors, *Biology Direct*, **6** (2011), 64, URL <http://biologydirect.biomedcentral.com/articles/10.1186/1745-6150-6-64>.
13. M. Kot, *Elements of mathematical ecology*, Cambridge University Press, 2001, URL <https://www.cambridge.org/us/academic/subjects/life-sciences/ecology-and-conservation/elements-mathematical-ecology?format=PB&isbn=9780521001502>.
14. Y. Kuang, J. D. Nagy and S. E. Eikenberry, *Introduction to mathematical oncology*, Chapman and Hall/CRC.
15. A. Madzvamuse, R. Barreira and A. Gerisch, Cross-Diffusion in Reaction-Diffusion Models: Analysis, Numerics, and Applications, Springer, Cham, 2017, 385–392, URL http://link.springer.com/10.1007/978-3-319-63082-3_{_}61.
16. N. L. Martirosyan, E. M. Rutter, W. L. Ramey, E. J. Kostelich, Y. Kuang and M. C. Preul, Mathematically modeling the biological properties of gliomas: A review, *Mathematical Biosciences and Engineering*, **12** (2015), 879–905, URL <http://aimsciences.org/journals/displayArticlesnew.jsp?paperID=11020>.
17. J. McDaniel, E. Kostelich, Y. Kuang, J. Nagy, M. C. Preul, N. Z. Moore and N. L. Martirosyan, Data Assimilation in Brain Tumor Models, Springer, New York, NY, 2013, 233–262, URL http://link.springer.com/10.1007/978-1-4614-4178-6_{_}9.
18. M. L. Neal, A. D. Trister, T. Cloke, R. Sodt, S. Ahn, A. L. Baldock, C. A. Bridge, A. Lai, T. F. Cloughesy, M. M. Mrugala, J. K. Rockhill, R. C. Rockne and K. R. Swanson, Discriminat-

- ing Survival Outcomes in Patients with Glioblastoma Using a Simulation-Based, Patient-Specific Response Metric, *PLoS ONE*, **8** (2013), e51951, URL <https://dx.plos.org/10.1371/journal.pone.0051951>.
19. A. D. Norden and P. Y. Wen, Glioma therapy in adults, *The neurologist*, **12** (2006), 279–92, URL <http://www.ncbi.nlm.nih.gov/pubmed/17122724>.
 20. J. A. Sherratt, Wavefront propagation in a competition equation with a new motility term modelling contact inhibition between cell populations, *Proceedings of the Royal Society of London. Series A: Mathematical, Physical and Engineering Sciences*, **456** (2000), 2365–2386, URL <http://www.royalsocietypublishing.org/doi/10.1098/rspa.2000.0616>.
 21. J. A. Sherratt and M. A. Chaplain, A new mathematical model for avascular tumour growth, *Journal of Mathematical Biology*, **43** (2001), 291–312, URL <http://link.springer.com/10.1007/s002850100088>.
 22. T. L. Stepien, E. M. Rutter and Y. Kuang, A data-motivated density-dependent diffusion model of in vitro glioblastoma growth., *Mathematical biosciences and engineering : MBE*, **12** (2015), 1157–72, URL <http://www.ncbi.nlm.nih.gov/pubmed/26775861>.
 23. T. L. Stepien, E. M. Rutter and Y. Kuang, Traveling Waves of a Go-or-Grow Model of Glioma Growth, *SIAM Journal on Applied Mathematics*, **78** (2018), 1778–1801, URL <https://epubs.siam.org/doi/10.1137/17M1146257>.
 24. R. Stupp, W. P. Mason, M. J. van den Bent, M. Weller, B. Fisher, M. J. Taphoorn, K. Belanger, A. A. Brandes, C. Marosi, U. Bogdahn, J. Curschmann, R. C. Janzer, S. K. Ludwin, T. Gorlia, A. Allgeier, D. Lacombe, J. G. Cairncross, E. Eisenhauer and R. O. Mirimanoff, Radiotherapy plus Concomitant and Adjuvant Temozolomide for Glioblastoma, *New England Journal of Medicine*, **352** (2005), 987–996, URL <http://www.nejm.org/doi/abs/10.1056/NEJMoa043330>.
 25. K. R. Swanson, R. C. Rockne, J. Claridge, M. A. Chaplain, E. C. Alvord and A. R. A. Anderson, Quantifying the Role of Angiogenesis in Malignant Progression of Gliomas: In Silico Modeling Integrates Imaging and Histology, *Cancer Research*, **71** (2011), 7366–7375, URL <http://www.ncbi.nlm.nih.gov/pubmed/21900399><http://www.pubmedcentral.nih.gov/articlerender.fcgi?artid=PMC3398690><http://cancerres.aacrjournals.org/cgi/doi/10.1158/0008-5472.CAN-11-1399>.
 26. K. R. Swanson, R. C. Rostomily and E. C. Alvord, A mathematical modelling tool for predicting survival of individual patients following resection of glioblastoma: a proof of principle, *British Journal of Cancer*, **98** (2008), 113–119, URL <http://www.nature.com/articles/6604125>.

Appendix

Traveling wave

The main purpose of this subsection is to rigorous establish the existence of traveling wave solutions in system (2.8). To this end, we first show that the solutions of system (2.8) with positive initial values are non-negative and bounded.

Lemma 1. Assume that $g(w) = wG(w)$ with $G(w)$ a bounded function. Then, the solutions of system (2.8) with positive initial values are positive and bounded.

Proof: Observe that if $x' = xf(t, x)$ where f is a bounded function, then $x(t) = x(t_0)e^{\int_{t_0}^t f(s, x(s))ds} > 0$. This implies the positivity of the solutions of system (2.8) with positive initial values. Since

$$\frac{d(p+w)}{dz} = -\delta(w), \quad (4.1)$$

we see that $(p+w)$ is bounded, which implies that both p and w are also bounded. \square

Observe that for any $w^* \in [0, 1]$, $(0, w^*)$ is an equilibrium of system (2.8).

Theorem 1. System (2.8) admits positive traveling wave solutions which correspond to the heteroclinic orbits connecting steady state $(0, 1)$ to another steady state $(0, w^*)$.

Proof: We perform a detailed phase plane (w - p plane, see Figure 1) analysis of (2.8) to show the existence of a trajectory that starts from $(1, 0)$ and ends at $(w^*, 0)$ where $w^* \in [0, 1]$. First we notice that

$$\frac{dp}{dw} = \frac{\delta(w)}{\hat{\rho}g(w)} - 1, \quad (4.2)$$

$$\frac{d^2p}{dw^2} = \frac{\delta'(w)g(w) - \delta(w)g'(w)}{\hat{\rho}g(w)^2}, \quad (4.3)$$

Since $g(w)$, $\delta(w)$ are both positive functions with $g'(w) > 0$ and $\delta'(w) < 0$ on $w \in [0, 1]$, thus $\frac{d^2p}{dw^2} < 0$ for all $w \in [0, 1]$.

We show first that the trajectory starts from $(1, 0)$ will never cross the line $p = 1 - w$.

Since $g(1) = 1$, $\delta(1) = 0$. we have $\frac{dp}{dw}|_{w=1} = -1$. Together with $\frac{d^2p}{dw^2} < 0$, we know that the trajectory with $w < 1$ will have slope greater than -1 , which means it won't cross the line $p = 1 - w$.

Since solution components stay positive, we see that the trajectory starts from $(1, 0)$ will never cross the p -axis from right to left.

Due to the monotonicity of the functions g and δ , it is easy to that there is a unique value w^\dagger in $(0, 1)$ such that $\frac{dp}{dw}|_{w=w^\dagger} = 0$. Moreover, $\frac{dp}{dw}|_{1>w>w^\dagger} > 0$ while $\frac{dp}{dw}|_{0<w<w^\dagger} < 0$.

Observe that w is strictly decreasing and bounded from below by 0, we conclude that there exists some $w^* \in (0, 1)$ such that, $\lim_{z \rightarrow \infty} w(z) = w^*$.

We claim that $w^* < w^\dagger$. Otherwise, we have p a non-decreasing function, implying the trajectory approaches a positive steady state $E^* = (p^*, w^*)$. However, system (2.8) does not admit any positive steady states.

Let $a \in (w^*, w^\dagger)$ and $b = \hat{\rho}g(a) - \delta(a) < 0$. Since $\lim_{z \rightarrow \infty} w(z) = w^*$, we see that there is a $z^* > 0$ such that for $z \geq z^*$, $w < a$. Therefore, for $z \geq z^*$, $\frac{dp}{dz} < bp$, implying that $\lim_{z \rightarrow \infty} p(z) = 0$. Hence, system (2.8) admits positive traveling wave solutions which correspond to the heteroclinic orbits connecting steady state $(0, 1)$ to another steady state $(0, w^*)$. \square

Rim width

The trajectory in Figure 1 corresponds to a traveling wave profile in z -coordinate as shown on the left pane of Figure 3. Because of our choice of nondimensionlization ($x = -\frac{2\sqrt{D\rho}}{k}z$), by definition we

have the rim width in dimensional form

$$\ell_1 = \frac{2\sqrt{D\rho}}{k}(z_1^+ - z_1^-) = \frac{2\sqrt{D\rho}}{k} \int_{z_1^-}^{z_1^+} dz$$

where $p(z_1^\pm) = a_1 p_{\max}$. Note that we have taken p as a function of z (see left pane of Figure 3). We can also take w as a function of z to make a change of variable to the above integral, resulting in (2.10a). Similar argument applies to (2.10b)

Derivation of R_1^ and R_2^**

Based on the assumption that from $t = 0$ to $t = t^*$, quiescence is negligible and the proliferating cell density grows exponentially, the governing equation of tumor cell density is

$$\frac{\partial p}{\partial t} = D \frac{1}{r^2} \frac{\partial}{\partial r} \left(r^2 \frac{\partial p}{\partial r} \right) + \rho p,$$

where spherical symmetry is used since spherical effect is important when tumor radius is small. This linear equation has a Green's function

$$p(r, t) = \frac{1}{(4\pi Dt)^{3/2}} e^{\rho t - \frac{r^2}{4Dt}}$$

(see, e.g., [13] Page 314 and [1] Page 285). Suppose that the tumor starts at $t = 0$ as a point source with density p_0 . It follows that at $t = t^*$, the position of tumor front at density $p = a_i$ is as (2.14).



AIMS Press

©2019 the Author(s), licensee AIMS Press. This is an open access article distributed under the terms of the Creative Commons Attribution License (<http://creativecommons.org/licenses/by/4.0>)